Transactions of Tianjin University (2023) 29:46–61
https://doi.org/10.1007/s12209-022-00339-6

RESEARCH ARTICLE

Li_2TiO_3 Dopant and Phosphate Coating Improve the Electrochemical Performance of $LiCoO_2$ at 3.0–4.6 V

Baozhao Shi[1] · Jiangli Feng[1] · Jing Liu[1] · Yanan Zhou[1] · Jinli Zhang[1,2] · Wei Li[1,2]

Received: 5 July 2022 / Revised: 11 August 2022 / Accepted: 25 August 2022 / Published online: 29 August 2022

Abstract

A sol–gel tandem with a solid-phase modification procedure was developed to synthesize Li_2TiO_3-doped $LiCoO_2$ together with phosphate coatings (denoted as LCO-Ti/P), which possesses excellent high-voltage performance in the range of 3.0–4.6 V. The characterizations of X-ray diffraction, high-resolution transmission electron microscopy, and X-ray photoelectron spectroscopy illustrated that the modified sample LCO-Ti/P had the dopant of monoclinic Li_2TiO_3 and amorphous Li_3PO_4 coating layers. LCO-Ti/P has an initial discharge capacity of 211.6 mAh/g at 0.1 C and a retention of 85.7% after 100 cycles at 1 C and 25 ± 1 °C between 3.0 and 4.6 V. Nyquist plots reflect that the charge transfer resistance of LCO-Ti/P after 100 cycles at 1 C is much lower than that of the spent LCO, which benefits Li-ion diffusion. Density functional theory calculations disclose the superior lattice-matching property of major crystal planes for Li_2TiO_3 and $LiCoO_2$, the lower energy barriers for Li-ion diffusion in Li_2TiO_3, and the suppressed oxygen release performance resulting from phosphate adsorption. This work provides useful guidance on the rational design of the high-voltage performance of modified $LiCoO_2$ materials in terms of lattice-matching properties aside from the phosphate coating to reduce the energy barriers of Li-ion diffusion and enhance cycling stability.

Keywords $LiCoO_2$ · High-voltage performance · Li_2TiO_3 · Lattice matching · Li-ion diffusion · Density functional theory calculation

Introduction

$LiCoO_2$ has been the dominant cathode material for lithium-ion batteries in portable electronic products because of its high volumetric energy density [1, 2]. Increasing the operating voltage of $LiCoO_2$ can effectively enhance its specific capacity; however, achieving stable cycling performance of $LiCoO_2$ at high voltage faces many challenges [3], including the adverse phase transition at an operating voltage above 4.5 V (vs. Li/Li^+) [4, 5], the lattice distortion caused by internal mechanical strain, the loss of oxygen, dissolution of cobalt and side reactions with the electrolyte [6, 7].

Extensive studies have been reported to optimize the intrinsic physical properties of $LiCoO_2$ via doping alien elements into its crystal structure, including Ti [8, 9], Al [10], Mg [11], and Cr [12] or to enhance the cycling stability via generating protective coating layers on the surface of $LiCoO_2$, including TiO_2 [13–15], Al_2O_3 [16–18], MgO [19], ZrO_2 [20, 21], $AlPO_4$ [22, 23], and Li_3PO_4 [24]. In particular, some lithium-containing oxides, such as $Li_4Ti_5O_{12}$ [25] and Li_2TiO_3 [26], are considered promising coating materials because of their good conductivity of Li ions. For instance, Shim et al. [27] prepared spinel $Li_4Ti_5O_{12}$ coating layers on $LiCoO_2$ in addition to Mg doping and reported that the modified $LiCoO_2$ sample showed an initial discharge capacity of 184.9 mAh/g (0.5 C) and good cycling stability of 76% after 50 cycles at 0.5 C (160 mA/g) and about 25 °C in the range of 3.0–4.5 V. Cui et al. [28] modified $LiCoO_2$ using Al doping together with Li_2TiO_3 coating, obtaining an initial discharge capacity of 166.43 mAh/g with a retention of 93.9% after 100 cycles at 1 C (200 mA/g, 3.0–4.5 V). However, whether Li_2TiO_3 can be doped into $LiCoO_2$ and

✉ Wei Li
liwei@tju.edu.cn

[1] School of Chemical Engineering and Technology, Tianjin University, Tianjin 300350, China

[2] Haihe Laboratory of Sustainable Chemical Transformations, Tianjin 300192, China

the corresponding effect on the Li-ion diffusion of the cathode materials remain open questions.

Moreover, chemically inert phosphate can inhibit the undesired reactions between active materials and electrolytes and suppress the growth of the resistance to Li-ion diffusion [29, 30]. For example, Wang et al. [31] constructed a composite surface on $LiCoO_2$ consisting of amorphous coating layers of $AlPO_4$ and Li_3PO_4 as well as Al and P doping, and the modified sample showed an initial discharge capacity of 214.1 mAh/g (27.4 mA/g) and a retention of 88.6% after 200 cycles under a current density of 137 mA/g and RT in the range of 3.0–4.6 V. Gu et al. [32] used a spray-drying method of $NH_4{\cdot}H_2PO_4$ to synthesize a phosphate-rich coating layer on $LiCoO_2$, reporting an initial capacity of 179.3 mAh/g (0.2 C) and a retention of 80.9% after 500 cycles at 1 C (140 mA/g) and RT in the range of 3.0–4.5 V. Hence, we are enlightened to explore an effective method for improving the high-voltage performance of $LiCoO_2$ via the Li_2TiO_3 dopant as well as a phosphate coating layer.

In this article, using the precursors of $Ti(OC_4H_9)_4$ and NaH_2PO_2, a sol–gel tandem with a solid-phase modification procedure was developed to synthesize the modified $LiCoO_2$ (denoted as LCO-Ti/P), which possesses excellent high-voltage performance in the range of 3.0–4.6 V. Based on the characterizations of X-ray diffraction (XRD), high-resolution transmission electron microscopy (HRTEM), X-ray photoelectron spectroscopy (XPS), in situ XRD, etc., illustrated that the modified sample LCO-Ti/P has a multiphase interface consisting of monoclinic Li_2TiO_3, spinel Co_3O_4, and amorphous Li_3PO_4 coating layers, leading to an initial discharge capacity of 211.6mAh/g (0.1 C) and a retention of 85.7% after 100 cycles at 1 C and RT, which is far superior to the individual-element modified samples LCO-Ti and LCO-P. This work provides useful guidance on the rational design of the high-voltage performance of $LiCoO_2$ with crystalline phases that match properly with the bulky, layered structure at the interface.

Experimental

Material Synthesis

Pristine $LiCoO_2$ (LCO) was provided by Kejing Materials Technology. Three types of modified samples were prepared, including the individual-element modified samples of LCO-Ti and LCO-P and the dual-element modified LCO-Ti/P. To prepare the sample with the modification of Ti (LCO-Ti), 4.0 g $LiCoO_2$ was added to 100 mL ethanol solution containing 0.4 mL tetrabutyl titanate ($Ti(OC_4H_9)_4$) (98.0%, Aladdin, Shanghai) and 0.4 mL acetic acid (36.0 wt%) under vigorous stirring at RT. After stirring for 12 h, the mixture was evaporated at 80 ℃, and then, the obtained powder was ground thoroughly, followed by calcination at 800 ℃ for 1 h at a heating rate of 5 ℃/min under the atmosphere. The final product was named LCO-Ti.

To prepare the sample with the modification of phosphorus (LCO-P), 4.0 g $LiCoO_2$ was mixed with 0.024 g NaH_2PO_2 (99.0%, Aladdin, Shanghai), i.e., the NaH_2PO_2 additive accounts for 0.6 wt%, ground in a mortar in the presence of a small amount of ethanol for 10 min, and then dried and heated at 200 ℃ for 1 h. The obtained modified sample was denoted as LCO-P.

The dual-element modified sample LCO-Ti/P was prepared based on the Ti-modified sample LCO-Ti. A 1.0 g LCO-Ti sample was mixed with 0.006 g NaH_2PO_2 (the mass fraction of NaH_2PO_2 is 0.6 wt%) and ground in the presence of a small amount of ethanol for 10 min. Then, the mixture was dried and heated at 200 ℃ for 1 h. The obtained sample was named as LCO-Ti/P.

Material Characterization

X-ray diffraction (XRD) (Rigaku Smartlab) was used to determine the crystal structures of the samples using Cu Kα radiation in a range of 15–70° with a scanning rate of 1°/min. General structure analysis system (GSAS) software was used for Rietveld refinement. X-ray photoelectron spectroscopy (XPS) (ThermoFisher Scientific K-Alpha$^+$) measurements were performed to detect the valence state of surface elements with the peak calibration by C 1 s (284.80 eV). Advantage software was used to fit the peaks of the XPS spectra. The surface morphology and microstructures of the samples were observed with scanning electron microscopy (SEM) (FEI Apreo S LoVac), high-resolution transmission electron microscopy (HRTEM) (JEOL JEM-F200), and energy-dispersive spectrometry (EDS). Fourier-transform infrared spectroscopy (FT-IR) measurements of prepared samples were performed using a Thermo Scientific Nicolet iZ10 spectrometer. The sample materials were well mixed with KBr for FT-IR experiments. Each sample was scanned in the wavenumber range of 400–4000 cm^{-1}. The in situ XRD patterns were collected with a scanning rate of 10°/min in the range of 15–70° in the charging and discharging process at 0.2 C (1 C = 200 mA/g).

Electrochemical Characterization

The electrochemical performance of the cathode material was tested using half-cells (CR-2032) with a Li metal anode. The cathode electrodes were prepared by mixing the active material, polyvinylidene fluoride, and carbon black (8:1:1 by weight) with N-methyl-1,2-pyrrolidone (NMP) solution. The solvent was evaporated at 120 °C overnight after casting the slurry on Al foil. The active mass loading of the cathode

material was approximately 2.5–2.8 mg/cm^2. The electrolyte consisted of 1 mol/L $LiPF_6$ dissolved in a mixture of EC, DEC, and EMC (1:1:1 by volume). Cycling and rate performance and galvanostatic intermittent titration technique (GITT) tests were conducted on a Land system (CT2001A) at 3.0–4.6 V and 25 ± 1 °C (RT). The half-cells were first activated for two cycles at 0.1 C, and then, the long-term cycles were performed at 1 C (1 C = 200 mA/g). Cyclic voltammetry (CV) and electrochemical impedance spectroscopy (EIS) tests were implemented on an electrochemical workstation (PARSTAT 4000A). The EIS test was conducted at a fully charged state (4.6 V) over a frequency range of 100 kHz–0.01 Hz, and CV tests were cycled from 3.0 to 4.6 V at a scan rate of 0.1 mV/s.

First-Principles Calculations

Based on the PAW method, DFT (density functional theory) calculations were performed using the VASP package [33]. The exchange–correlation between electrons was described by the PBE functional under the GGA method [34]. Hubbard U parameters of 4.91 and 5.0 eV were employed to treat the strongly correlated d-orbital electrons of Co and Ti, respectively, referring to previous studies [35]. The electronic wave functions were expanded in a plane-wave basis set with an energy cutoff of 520 eV. To obtain a stable structure, the structural geometry was optimized until the average force on each atom was < 0.05 eV/Å. A resolution of $2\pi \times 0.04$ Å^{-1} for the Monkhorst–Pack *k*-point mesh was used to integrate the Brillouin zone [36]. The nudge elastic band method was used to evaluate Li-ion diffusion pathways and the diffusion energy barrier [37].

The binding energies between the crystal planes of $LiCoO_2$ and Li_2TiO_3 were calculated using the following equation:

$$\Delta E = E(\mathrm{LCO{-}LTO}) - E(\mathrm{LCO}) - E(\mathrm{LTO}) \quad (1)$$

where E(LCO-LTO) represents the total energy of the system of interfacial structural models, and E(LCO) and E(LTO) represent the energies of the different crystal planes of $LiCoO_2$ and Li_2TiO_3, respectively.

The PO_4^{3-} adsorption energy was calculated using the following formula:

$$E_{\mathrm{adsorption}} = E(\mathrm{LCO{-}PO_4^{3-}}) - E(\mathrm{LCO}) - E(\mathrm{PO_4^{3-}}) \quad (2)$$

where E(LCO–PO_4^{3-}) indicates the total energy of the LiCoO2 system with the adsorbed PO_4^{3-}, E(LCO) is the total energy of LiCoO2, and E(PO_4^{3-}) represents the energy of PO_4^{3-}.

The oxygen vacancy formation energy was defined as follows.

$$E_{\mathrm{Oxygen\ vacancy}} = E(\mathrm{LCO{-}}O) + 1/2E(O_2) - E(\mathrm{LCO}) \quad (3)$$

where E(LCO–O) represents the total energy of $LiCoO_2$ with one oxygen vacancy, E(LCO) is the total energy of LiCoO2, and E(O_2) indicates the energy of an oxygen molecule.

Results

XRD patterns were recorded to determine the crystal structures of pristine LCO and the modified sample (LCO-Ti/P) together with the control samples with single-element modification (LCO-P, LCO-Ti). As shown in Fig. 1a, the main structures of all the samples are classified as the α-$NaFeO_2$-type layered structure (JCPDS: 50–0653) with an R-3 m space group. Notably, for LCO-Ti and LCO-Ti/P, small peaks appear at 31.27° and 36.85°, which are indexed to spinel Co_3O_4 (JCPDS: 42–1467) with a space group of Fd-3 m, as well as the peak at 43.72°, which is indexed to monoclinic Li_2TiO_3 (JCPDS: 33–0831) with a space group of C 2/c. The Rietveld refinement patterns of these samples are given in Fig. 1b, c, and Fig. S1, respectively, and the corresponding lattice parameters are listed in Table 1. The *c*/*a* values of all samples are > 4.9, indicating a well-ordered layered structure.

The morphologies of all samples were observed through SEM images. As shown in Fig. S2, the pristine LCO sample has a smooth and clean surface, whereas the surfaces of the modified samples (LCO-P, LCO-Ti, and LCO-Ti/P) are rough to some extent, suggesting that coating layers were formed on the surfaces.

HRTEM images were observed to disclose the phase compositions of LCO and LCO-Ti/P. As shown in Fig. 2a, pristine LCO exhibits a uniform crystal phase with a layered structure. The fast Fourier transform (FFT) pattern in Region 1 shows the (104), (110), and (1–4) planes of the layered phase (R-3 m), and the lattice spacing of 0.21 nm corresponds to the (104) plane. In Region 2, the FFT pattern shows the (012) planes of the layered phase (R-3 m), and the lattice spacing of 0.23 nm also corresponds to the (012) plane. However, LCO-Ti/P has a multiphase surface structure (Fig. 2b). The FFT pattern of the inner area of LCO-Ti/P (cyan dashed rectangle in Region 2) shows the layered phase (R-3 m) in the bulk area, and the lattice spacing of 0.21 nm corresponds to the (104) plane of the layered phase. In contrast, the yellow dashed rectangle in Region 2 corresponds to the monoclinic phase (C2/c) of Li_2TiO_3, the FFT pattern shows the (33–1), (− 206), and (135) planes, and the lattice spacing of 0.15 nm is near the interplanar distance of the (− 206) plane of monoclinic Li_2TiO_3. In Region 1, the diffraction pattern of the surface structure (green dashed rectangle) shows an identifiable spinel structural feature with an FFT pattern due to the (400), (040), and (440) planes, and the lattice spacing of 0.22 nm approximates

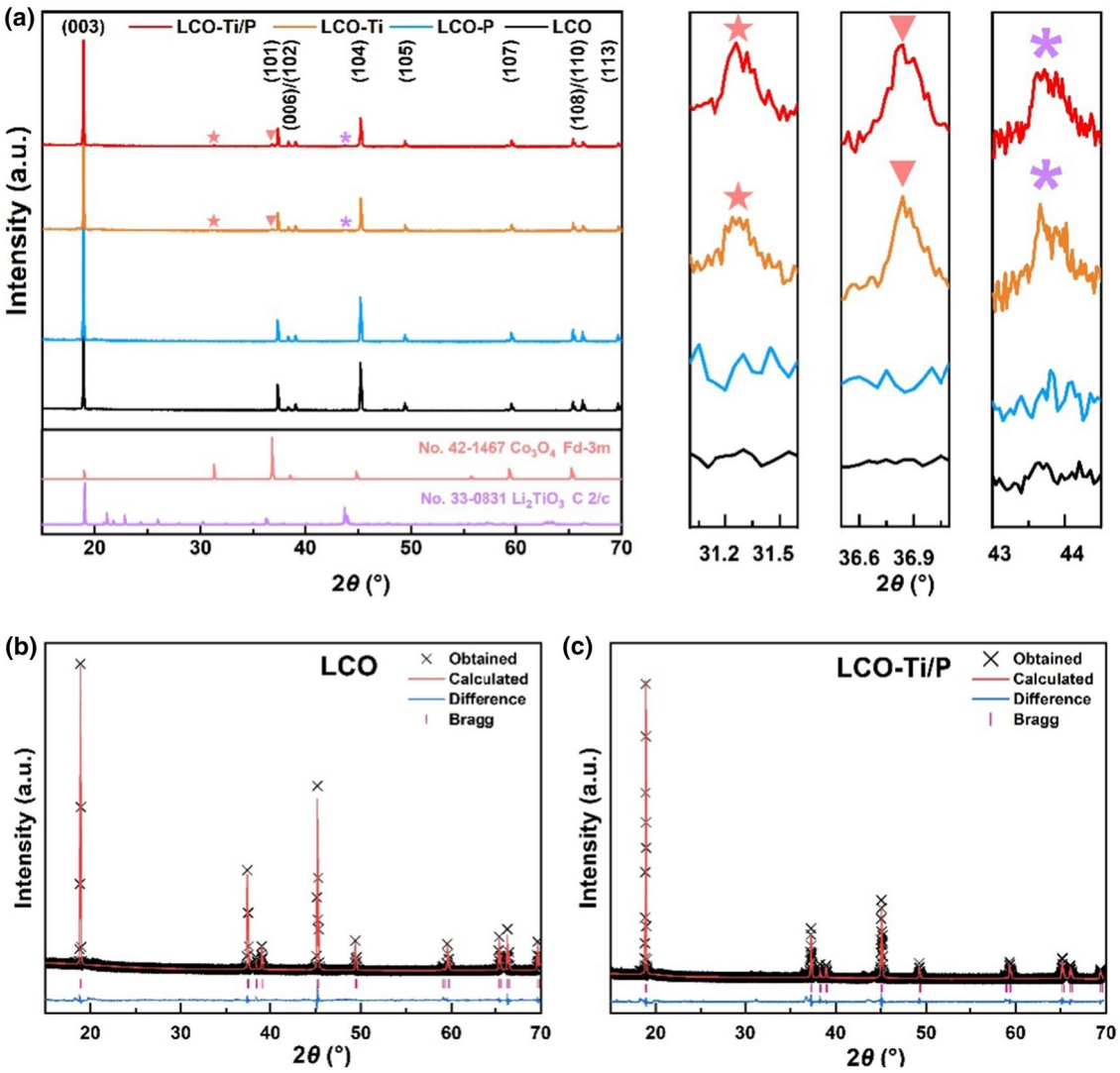

Fig. 1 **a** XRD patterns and the enlarged views of all samples. Rietveld refinements for **b** LCO and **c** LCO-Ti/P

Table 1 Refined crystallographic parameters of all samples

Samples	*a*/Å	*c*/Å	*c*/*a*	*V*/Å^3	R_{wp}/%	R_p/%
LCO	2.8166	14.0573	4.9908	96.58	1.8	1.3
LCO-P	2.8182	14.0646	4.9907	96.74	3.5	2.6
LCO-Ti	2.8262	14.1057	4.9910	97.58	3.9	2.7
LCO-Ti/P	2.8262	14.1045	4.9906	97.57	4.3	2.9

the interplanar distance of the (400) plane of spinel Co_3O_4. These results agree with the above XRD results, confirming the presence of spinel $Co_3O_4$and monoclinic Li_2TiO_3 in the modified LCO-Ti/P sample. In the area of the outmost surface of LCO-Ti/P (marked by the red dashed line in Region 2), an amorphous phase layer is observed. The amorphous phase is probably due to Li_3PO_4, according to the synthetic process, which is confirmed by XPS spectra in this context. EDS spectra of LCO-Ti/P were obtained to detect the uniformity of the Ti and P elements on the surface, as shown in Fig. S3, suggesting the uniform distribution of Ti and P elements in LCO-Ti/P.

XPS spectra were recorded to distinguish the surface compositions and identify the valence states of elements. For the individual-element modified sample LCO-Ti, in the Ti 2p XPS spectra (Fig. 3a), the peaks at the binding energies of 458.28 eV and 464.08 eV correspond to Ti^{4+} [38], which agrees with the above results of Li_2TiO_3 reflected by XRD

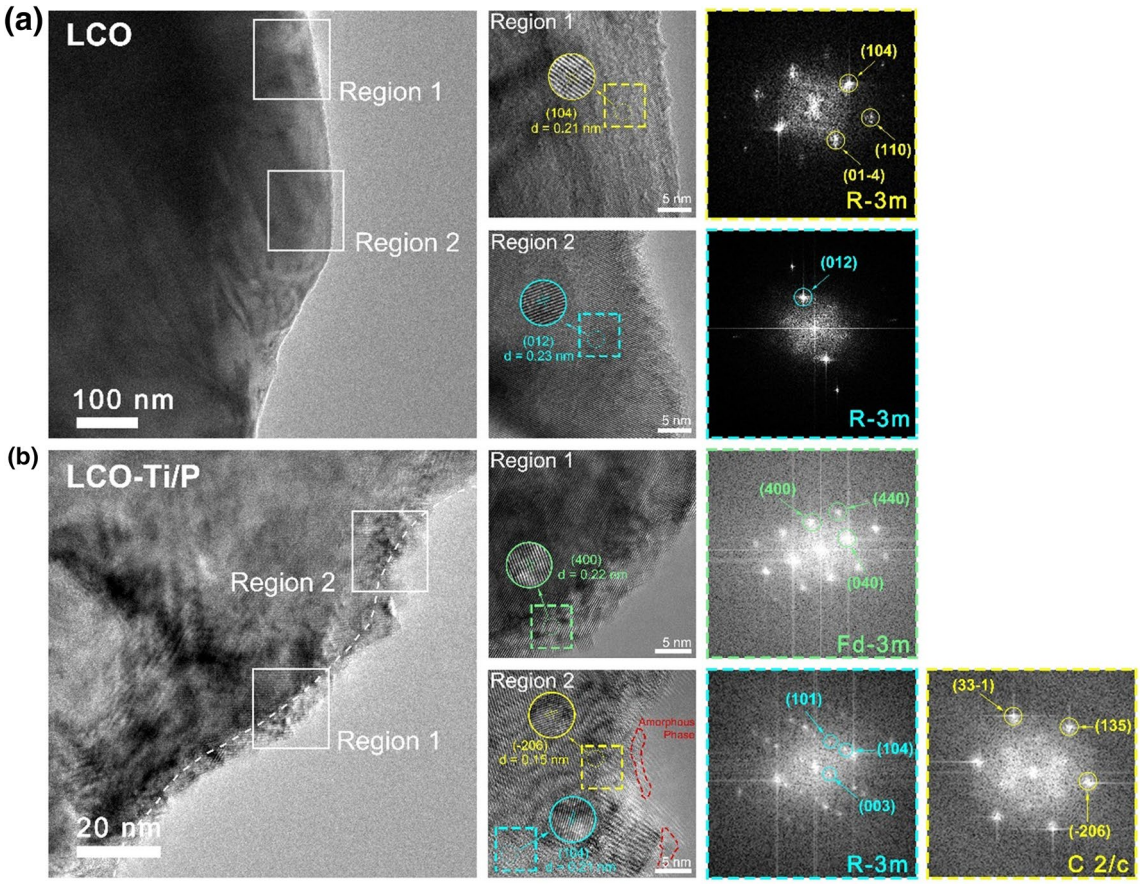

Fig. 2 HRTEM images and the corresponding FFT patterns of **a** LCO and **b** LCO-Ti/P

and HRTEM analyses. For the dual-element modified sample LCO-Ti/P, Ti 2pXPS spectra have similar peak positions with those of LCO-Ti, in addition to the slight shifts of binding energies, which are probably caused by the influence of PO_4^{3-}. In the case of the P 2p XPS spectra, LCO-Ti/P and LCO-P have a peak at 132.78 eV (Fig. 3b), corresponding to the P−O bonding of PO_4^{3-} [39, 40].

Figure 3c displays the O 1 s XPS spectra of the modified samples, exhibiting peaks at 533.17 and 532.00 eV assigned to C−O and C=O bonds, peaks near 529.10 and 529.50 eV assigned to the lattice oxygen, and a peak at 531.04 eV due to overlapping Ti−O (531.40 eV for LCO-Ti) and P−O (530.80 eV for LCO-P) peaks [41, 42]. Table S2 lists the relative percentages of different oxygen species and the binding energies of these four samples. The O 1 s peaks of LCO-Ti have high intensities, probably due to the greater amount of hydrolyzed product from the Ti-precursor on the surface. As for Co 2p XPS spectra (Fig. 3d and Table S3), these four samples have similar binding energies for Co^{2+} 2p3/2 and Co^{3+} 2p3/2 [43]. In combination with XRD and HRTEM results, this result suggests that the modified sample LCO-Ti/P has a Li_2TiO_3 dopant as well as a Li_3PO_4 coating layer.

The FT-IR spectra of LCO and LCO-Ti/P were recorded, as shown in Fig. S2. The bands at 550 and 600 cm^{-1} correspond to CoO_6 stretching and bending vibrations [44], the broad bands near 1630 cm^{-1} and 3400 cm^{-1} are assigned to adsorbed water molecules, and the bands near 1100 cm^{-1} correspond to the C=O vibration due to the adsorption of CO_2 [45]. Notably, additional characteristic peaks appear from 900 to 1100 cm^{-1} in the LCO-Ti/P spectrum, and the small absorption peaks at 1050, 1085, and 1180 cm^{-1} are due to asymmetric P−O stretching vibrations and asymmetrical stretching of P=O in PO_4^{3-}, confirming the formation of Li_3PO_4 [46, 47].

The electrochemical performances of the individual-element modified samples of LCO-Ti and LCO-P and the dual-element modified LCO-Ti/P were evaluated by galvanostatic tests in the range of 3.0–4.6 V. As shown in Fig. 4a, the initial discharge capacities of LCO, LCO-Ti, LCO-P, and LCO-Ti/P at RT and 0.1 C are 214.5, 212.3, 213.6, and 211.6 mAh/g, respectively. After 100 cycles at 1 C, LCO, LCO-Ti, LCO-P, and LCO-Ti/P show capacity retention of 27.4%, 65.5%, 65.9%, and 85.7%, respectively. After 300 cycles at 1 C, LCO-Ti/P maintains a capacity of 130.4 mAh/g, i.e., having a retention of 67.3%, far superior

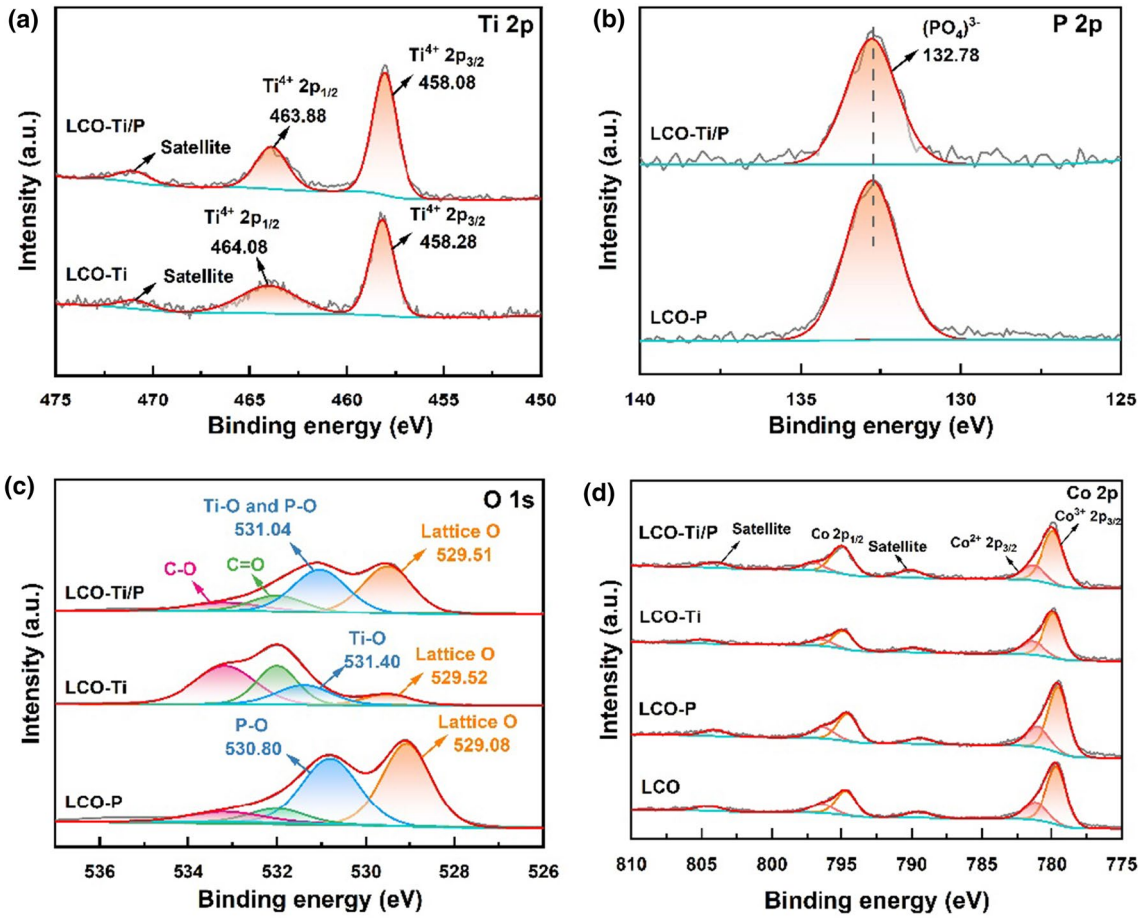

Fig. 3 **a** Ti 2p XPS spectra of LCO and LCO-Ti/P. **b** P 2p XPS spectra of LCO-P and LCO-Ti/P. **c** O 1 s and **d** Co 2p XPS spectra of all samples

to pristine LCO and the individual-element modified samples (LCO-Ti, LCO-P). Table S1 compares the high-voltage electrochemical performance of LCO-Ti/P with that of the modified $LiCoO_2$ material published in the recent literature. The dual-element modified sample LCO-Ti/P shows a comparable high-voltage performance.

Figure 4b displays the rate capabilities of LCO-Ti/P and LCO. LCO-Ti/P delivers a higher capacity under high current density, and a reversible capacity of 199.7 mAh/g with retention of 97.5% is achieved while returning to 0.1 C, indicating that the dual-element modification can provide a fast Li-ion diffusion pathway. The charge/discharge profiles at the selected cycle numbers are presented in Fig. 4c, d. Pristine LCO shows severely degraded profiles compared with LCO-Ti/P, and the corresponding discharge voltage fading during cycling is shown in Fig. S4. Rapid voltage fading is caused by severe structural degradation. The ameliorative voltage decay of LCO-Ti/P indicates that the dual-element modification can efficaciously stabilize the crystal structure during Li-ion deintercalation and intercalation.

CV curves within the first five cycles for these samples are compared in Fig. 5. All samples have redox peaks near 3.8 V and 4.4 V, which correspond to the H2/H1 and M2/H3 phase transitions, respectively [48]. For pristine LCO, these peaks gradually weaken with the scanning cycles (Fig. 5a), and similar trends appear for LCO-Ti and LCO-P (Fig. 5b, c). The broadened redox peaks in LCO-P (Fig. 5b) indicate suppressed charge transfer kinetics due to the low electronic conductivity of Li_3PO_4. In the case of LCO-Ti/P, slight decreases in the peak intensities are apparent (Fig. 5d), suggesting a reversible phase transition. Additionally, the potential difference between the main redox peaks in the first cycle for LCO-Ti/P equals 0.202, which is smaller than that of LCO (0.222), reflecting the lower polarization of LCO-Ti/P compared with pristine LCO. The lower polarization leads to a better electrochemical property; therefore, LCO-Ti/P possesses excellent cycling stability.

In situ XRD patterns were tested for LCO and LCO-Ti/P during the first cycle in the range of 3.0–4.6 V at 0.2 C. The evolution of the (003) and (107) diffraction peaks of LCO and LCO-Ti/P is shown in Fig. 6a, b, respectively. The

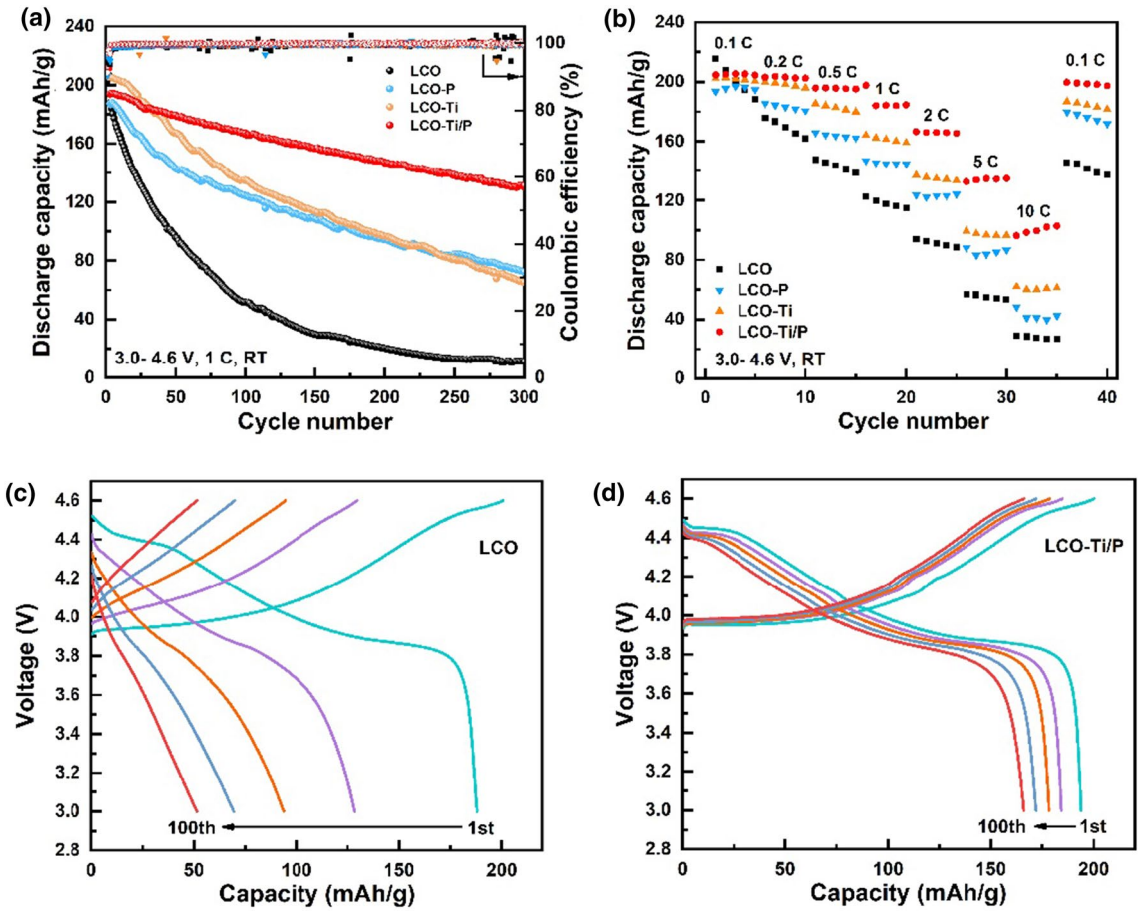

Fig. 4 **a** Cycling stability performances and Coulombic efficiencies of LCO, LCO-Ti, LCO-P, and LCO-Ti/P in the range of 3.0–4.6 V at 1 C and RT. **b** Rate performances of LCO, LCO-Ti, LCO-P, and LCO-Ti/P at RT (3.0–4.6 V). Charge/discharge profiles of **c** LCO and **d** LCO-Ti/P (3.0–4.6 V) at 1 C and RT (1st, 25th, 50th, 75th, and 100.th cycles)

insulator–metal two-phase transition at the beginning of the charging stage leads to the splitting of (003) and (107) peaks [49]. The order–disorder transition process at 4.2 V can be observed in LCO-Ti/P, featuring (107) peak splitting [50]; however, this transition process disappears in the case of LCO, and this phenomenon agrees with the disappearance of anodic and cathodic peaks at 4.2 V in the CV curves of LCO (Fig. 5a), suggesting that LCO-Ti/P possesses high structural reversibility. When the voltage is charged to 4.6 V, the phase transition from O3 to H1–3 is observed in the (003) peak evolution pattern, and the variation in the c-value during the phase transition is reflected in the amplitude of the (003) peak variation. LCO has a larger amplitude (1.277°) than LCO-Ti/P (1.222°), demonstrating the mitigation of structural change for LCO-Ti/P under high voltage. To obtain more detailed structure variations during charging and discharging, Rietveld refinements of in situ XRD were obtained, as shown in Fig. 6c. With the deintercalation and intercalation of Li ions, the lattice parameter, c-value, and volume value change significantly, and LCO-Ti/P exhibits less structural variation than that of LCO, indicating that dual-element modification can alleviate the structure deterioration [51, 52].

EIS was performed to analyze the kinetic behaviors of these samples. Nyquist plots are shown in Fig. 7a, b, and Fig. S6, respectively, and the fitting results by the Zview2 software are shown in Table 2 and Table S4. The intersection of the starting point and the x-axis in the Nyquist plots represents the ohmic resistance (R_s), and the semicircles at high frequency and medium frequency represent the electrode surface film impedance (R_f) and charge transfer impedance (R_{ct}), respectively; the sloping line at low frequency reflects the Li-ion solid-state diffusion (W_o) [53]. The transfer kinetics at the interface can be reflected by the change in R_{ct}, and the reduced charge transfer resistance benefits Li-ion diffusion [54]. The growth of R_{ct} is significant for LCO, and R_{ct} drastically increases to 1412.00 Ω after 50 cycles at a high voltage of 4.6 V. The suppressed growth of R_{ct} for LCO-Ti and LCO-P is visually displayed in Fig. 7c, and concrete numerical results are listed

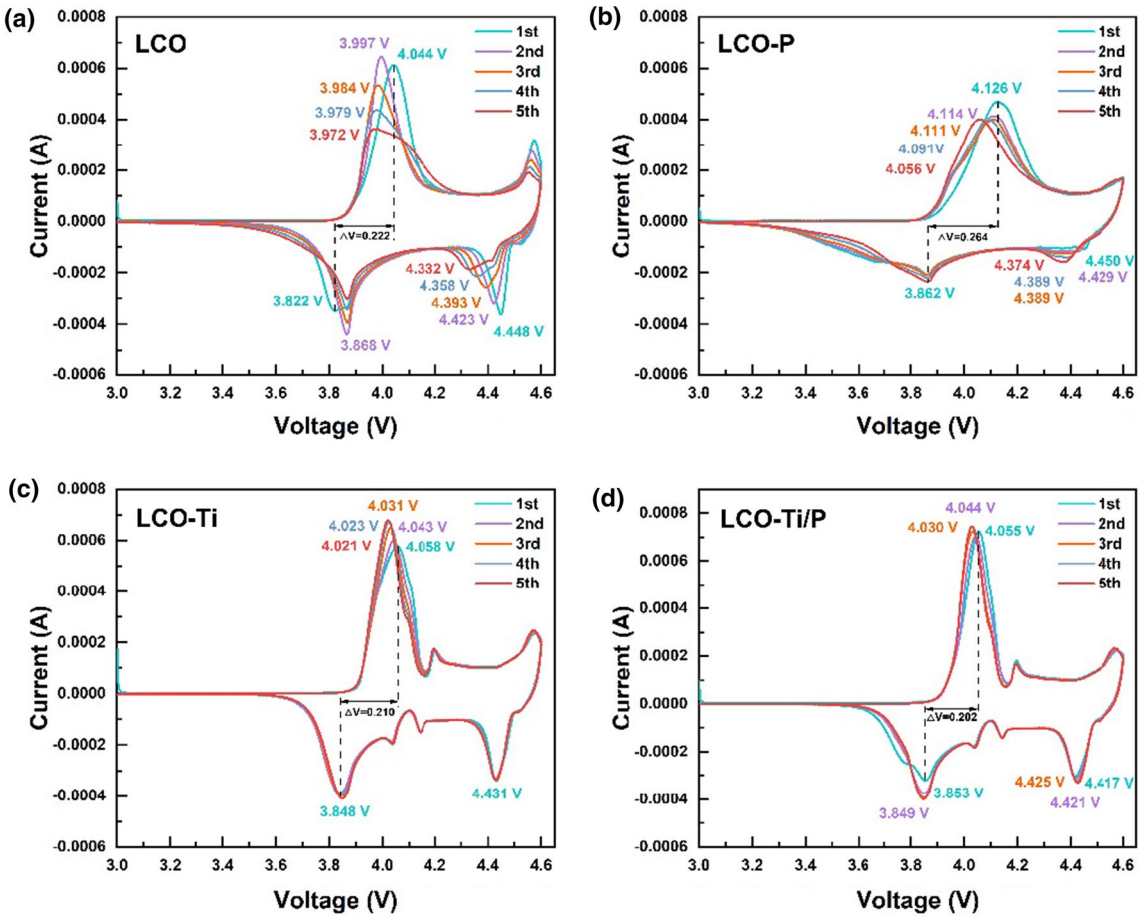

Fig. 5 Cyclic voltammetry of **a** LCO, **b** LCO-P, **c** LCO-Ti, and **d** LCO-Ti/P

in Table S4. Although R_{ct} gently increases to 675.20 for LCO-Ti/P (Table 2), the smaller variation in R_{ct} in cycling is due to the special surface structure resulting from the dual-element modification.

GITT characterizations were conducted for all samples during the 1st and 100th cycles, as shown in Fig. 7d and Fig. S7, respectively. The analysis details are shown in Supporting Information. The GITT result during the 1st cycle shows that the Li-ion diffusion coefficients of LCO-Ti/P and pristine LCO are almost identical, slightly higher than that of LCO-P, and lower than that of LCO-Ti. After 100 cycles, LCO-Ti/P shows a slightly reduced Li-ion diffusion coefficient compared with the first cycle, indicating that the dual-element modification generates a superior interfacial structure that can provide a fast Li-ion diffusion pathway. Moreover, the measurably reduced charge transfer resistance and unimproved Li-ion diffusion kinetics of LCO-P probably originate from the amorphous Li_3PO_4 coating layer, which is chemically inert to the electrolyte [55, 56].

Characterizations of the spent samples were performed for LCO and LCO-Ti/P after 100 cycles in the range of 3.0–4.6 V at 1 C. SEM images of spent LCO after 100 cycles show an obvious disintegration of particles (Fig. 8a), whereas spent LCO-Ti/P has intact particles with dense cathode electrolyte interphase (CEI) layers formed on the surface (Fig. 8b). The accumulated stress originating from anisotropic expansion and contraction of the lattice during the deep lithiation/delithiation process leads to the fragmentation of the particles, whereas after dual-element modification, the structural deterioration of LCO-Ti/P is alleviated. Figure 8c, d shows the HRTEM images of spent LCO and LCO-Ti/P, respectively. The LCO surface (Fig. 8c) reconstructs extensively and forms a large area of Co_3O_4-like spinel structure (dashed cyan rectangle in Region 1 and dashed green rectangle in Region 2) under long-term cycling due to oxygen loss and cobalt dissolution. The irreversible phase transition leads to rapid capacity decay [57, 58]. In contrast, the layered structure with a space group of R-3 m (Region 2) still dominates the crystal structure of LCO-Ti/P (Fig. 8d). The lattice fringe of 0.47 nm in the bulk corresponds to atypical (003) plane of the R-3 m layered structure. The FFT pattern of the outermost surface in Region 1 shows the (0–24), (113), and (13–1) planes of monoclinic Li_2TiO_3, and the amorphous phase (marked by a

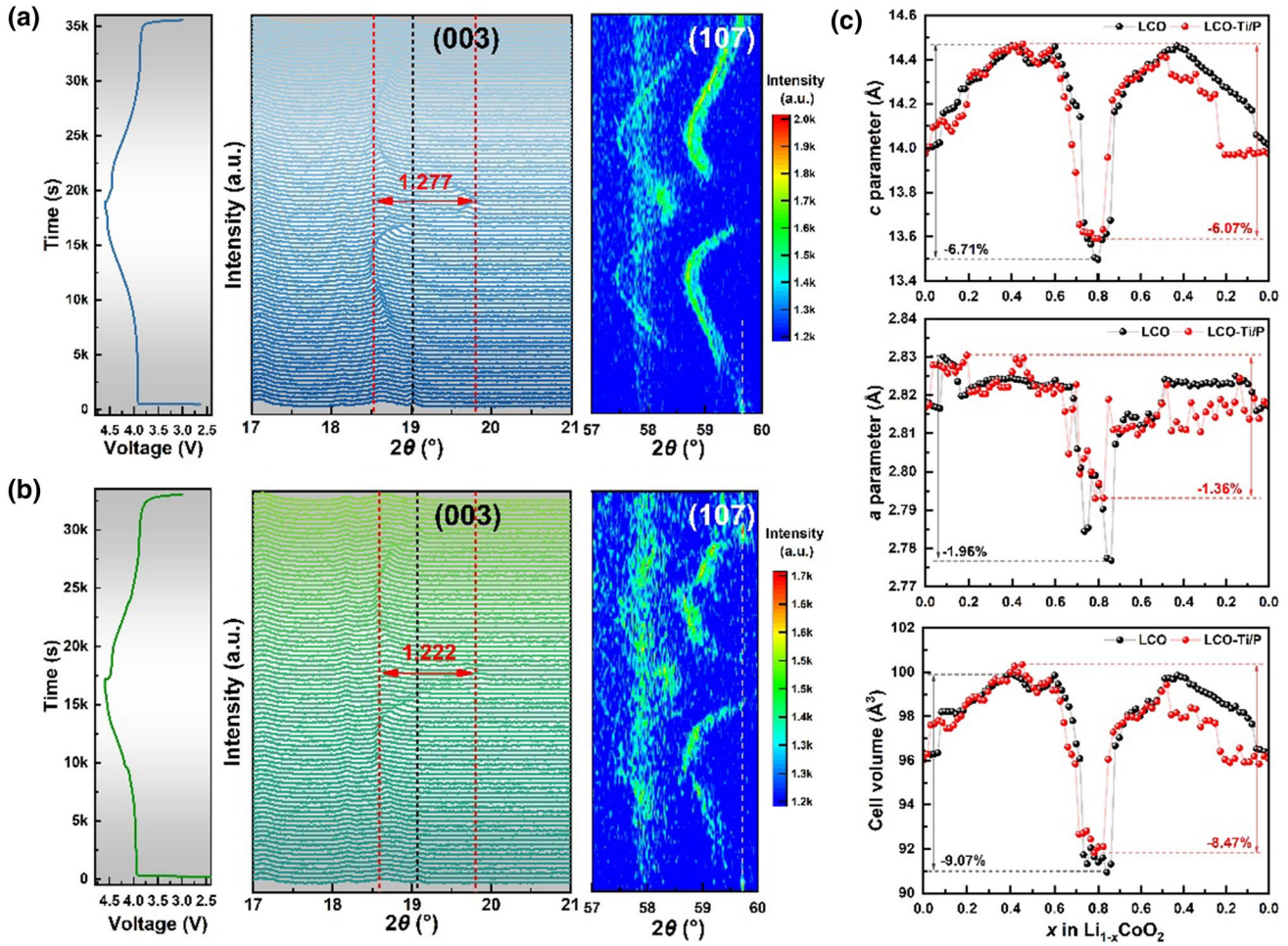

Fig. 6 Evolution of (003) and (107) diffraction peaks and the corresponding charge/discharge profiles of **a** LCO and **b** LCO-Ti/P during the first cycle in the range of 3.0–4.6 V at 0.2 C. **c** Corresponding changes in lattice parameters and cell volume

dashed red line) in the coating layer on the surface of LCO-Ti/P can be identified as Li_3PO_4, indicating a coating layer tightly attached to the bulk during cycling. In addition, the microcrack formation can be observed in the spent LCO, whereas no microcracks appear in the spent LCO-Ti/P. The robust coating layer hinders the direct contact of LCO with electrolytes, thus suppressing the side reaction originating from the electrolyte decomposition, and the oxygen loss and cobalt dissolution are effectively inhibited at high voltage. The optimized interfacial structure leads to the suppressed growth of charge transfer resistance, thus improving the cycling stability.

Discussion

The characterizations of XRD (Fig. 1), HRTEM (Fig. 2), and XPS (Fig. 3) illustrate that at the interface of the modified sample LCO-Ti/P, monoclinic Li_2TiO_3 and phosphate coatings are present. To further analyze the mechanism of dual-element modification, DFT calculations were performed to explain the improved cycling stability of LCO-Ti/P.

First, the lattice-matching property between monoclinic Li_2TiO_3 and layered $LiCoO_2$ was analyzed by calculating the binding energies of the individual crystal planes of these two materials. Figure 9a shows the interfacial structure models of the Li_2TiO_3(002) and $LiCoO_2$(003) crystal planes. The binding energy between these two crystal planes is calculated as −17.49 eV, which suggests a strong affinity between them. Shim et al. [27] analyzed the microstructure of $LiCoO_2$ modified by tetrabutyl titanate precursor through HAADF-STEM and found that the coating of monoclinic Li_2TiO_3 with space group C2/c was epitaxially grown on the $LiCoO_2$ surface, and the (003) planes of $LiCoO_2$ matched the (002) planes of Li_2TiO_3, which agreed with the simulation results.

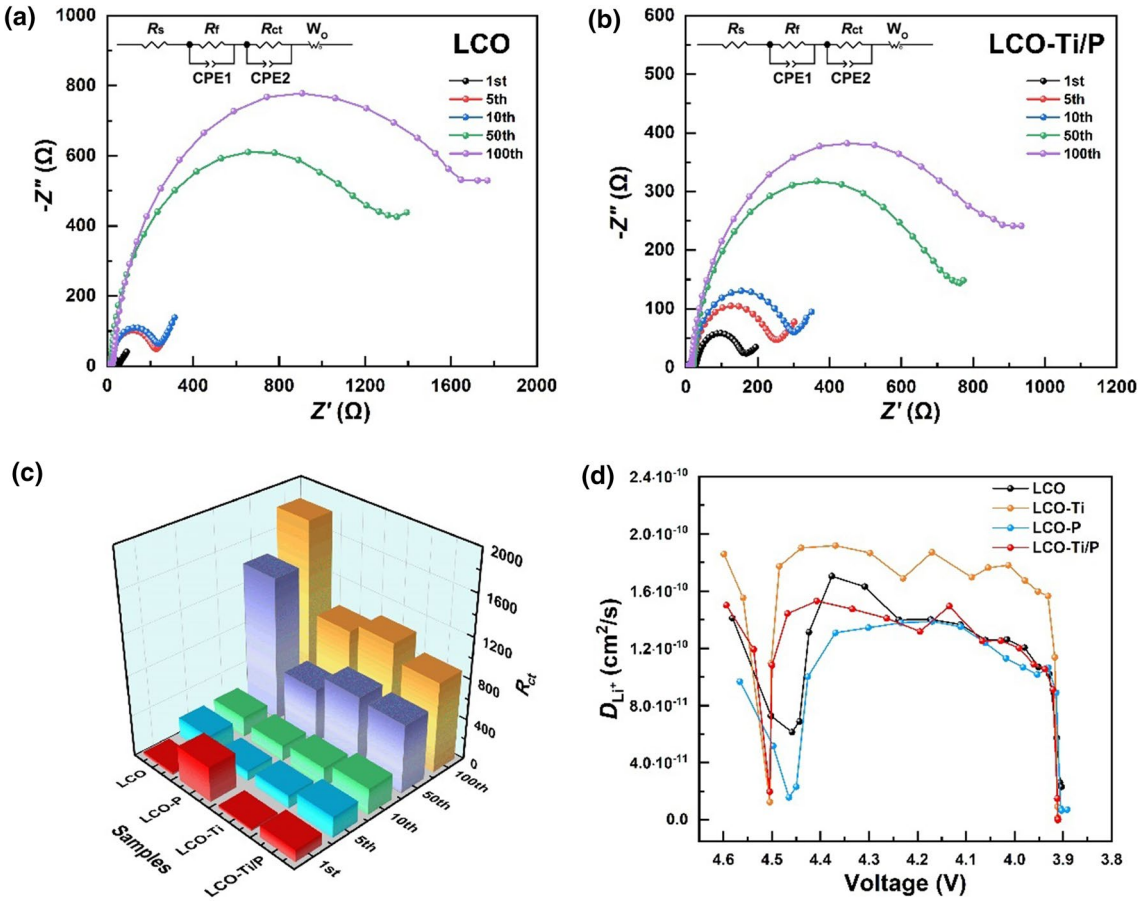

Fig. 7 EIS spectra of **a** LCO and **b** LCO-Ti/P based on the 1st, 5th, 10th, 50th, and 100th cycles and **c** comparison of R_{ct} of all samples. **d** D_{Li}^{+} calculated from GITT during the 1st cycle of the discharging process of all samples

Table 2 EIS fitting results of LCO and LCO-Ti/P

Samples	Cycle number	R_s (Ω)	R_f (Ω)	R_{ct}(Ω)	Samples	Cycle number	R_s (Ω)	R_f (Ω)	R_{ct}(Ω)
LCO	1st	2.88	19.54	29.78	LCO-Ti/P	1st	2.93	25.65	116.90
	5th	2.37	12.24	194.40		5th	3.72	15.43	206.60
	10th	2.82	13.36	200.80		10th	4.75	14.06	259.50
	50th	2.97	14.19	1421.00		50th	4.70	16.68	675.20
	100th	1.25	28.41	1825.00		100th	1.23	15.51	889.20

In addition, the lattice matching for the Li_2TiO_3(202) and $LiCoO_2$(104) crystal planes is spontaneous (Fig. 9b), with a calculated binding energy of − 10.9 eV. Similarly, Fig. S8 shows the interfacial structure models of matched crystal planes, including Li_2TiO_3(002) and $LiCoO_2$(104) as well as Li_2TiO_3(202) and $LiCoO_2$(003). The corresponding binding energies of these matched crystal planes are negative, as shown in Fig. 9c, illustrating that the major crystal planes of monoclinic Li_2TiO_3 and layered $LiCoO_2$ match perfectly. This excellent lattice matching between $LiCoO_2$ and Li_2TiO_3 is beneficial for achieving the superior structural stability of the cathode material by inhibiting particle cracking and breakage.

Moreover, the GITT results (Fig. 7d) indicate that LCO-Ti has the highest Li-ion diffusion coefficients. Herein, the effects of Li_2TiO_3 on the Li-ion diffusion energy barriers were investigated using molecular simulation. For pristine $LiCoO_2$, as shown in Fig. 10a, there are two Li-ion diffusion paths in $LiCoO_2$ [59, 60]: (1) Li ions diffuse through the adjacent octahedra in the Li–O layer (oxygen dumbbell hopping, ODH path), and (2) Li ions migrate among the octahedra through the intermediate tetrahedra (tetrahedral site hopping path, TSH path). Figure 10b indicates that in

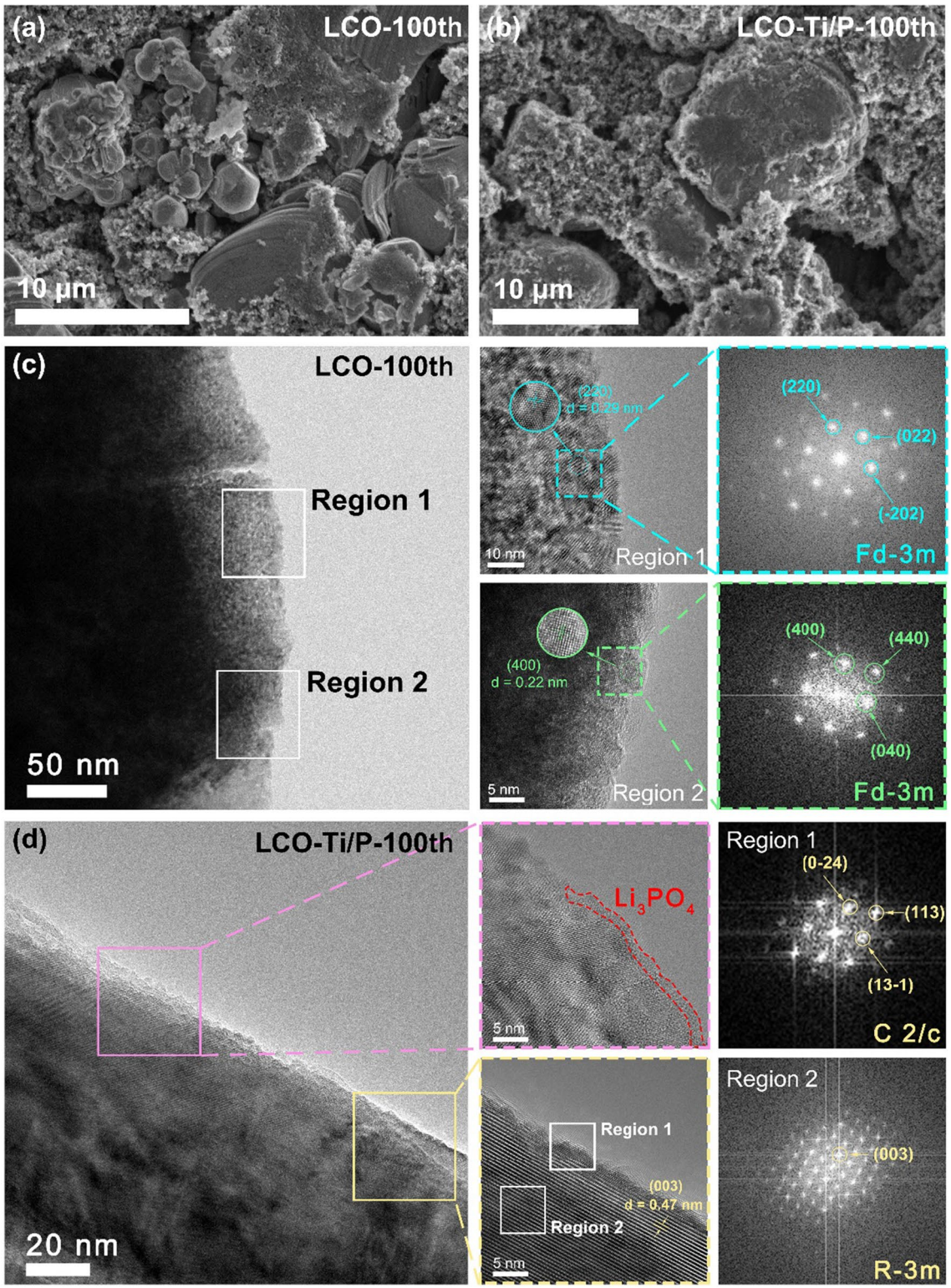

Fig. 8 SEM images of the spent samples of **a** LCO and **b** LCO-Ti/P after 100 cycles in the range of 3.0–4.6 V at 1 C. HRTEM images and the corresponding FFT patterns of the spent samples of **c** LCO and **d** LCO-Ti/P

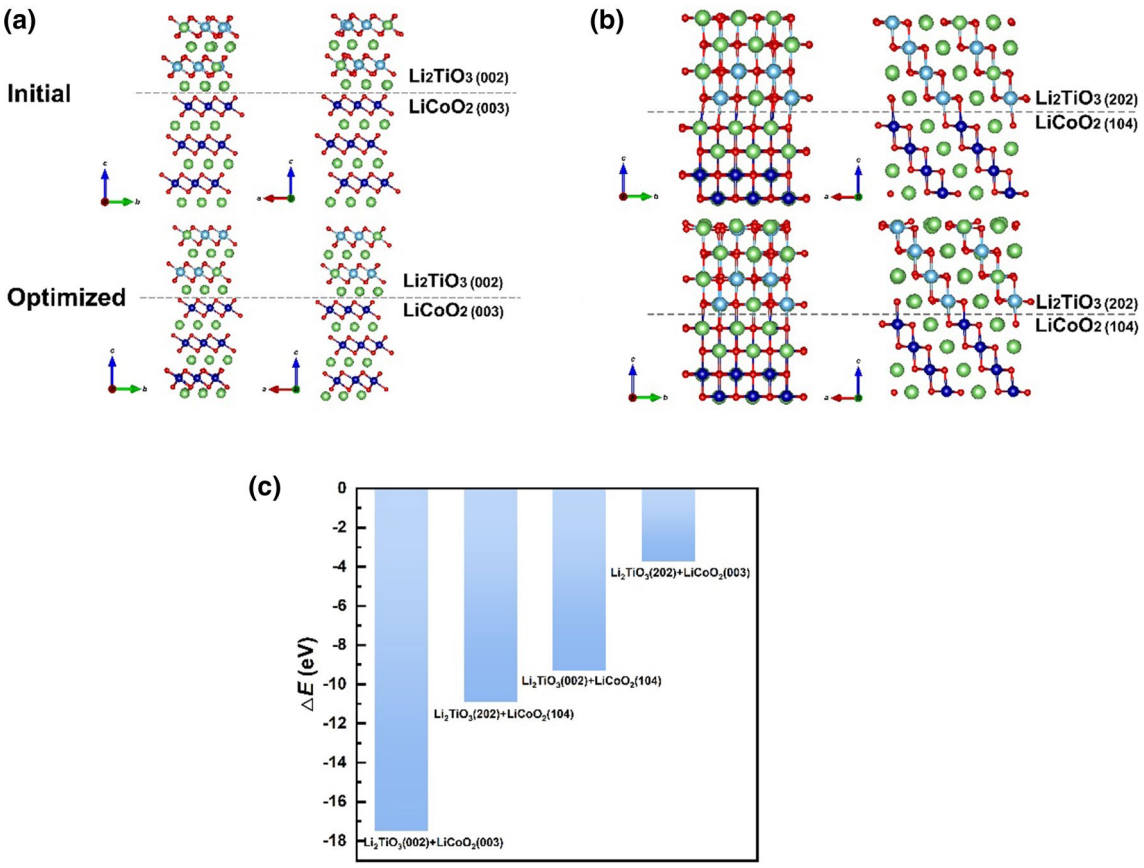

Fig. 9 Interfacial structure models of matched crystal planes between Li_2TiO_3 and $LiCoO_2$: **a** Li_2TiO_3(002) and $LiCoO_2$(003) and **b** Li_2TiO_3(202) and $LiCoO_2$(104). **c** Binding energies of major crystal planes between Li_2TiO_3 and $LiCoO_2$

pristine $LiCoO_2$, the Li-ion diffusion energy barrier is lower through the ODH path (0.68 eV) than through the TSH path.

For monoclinic Li_2TiO_3, there exists a 3D Li-ion diffusion path, i.e., Li ions can migrate through the Li–O and Ti–O layers, as displayed in Fig. 10c, e. Li_2TiO_3 has a lower Li-ion diffusion energy barrier through the Li–O layer (0.48 eV) (Fig. 10d) and the Ti–O layer (0.46 eV) (Fig. 10f), suggesting faster Li-ion diffusion in Li_2TiO_3 compared with $LiCoO_2$. Therefore, the 3D Li-ion diffusion in monoclinic Li_2TiO_3 results in a higher Li-ion diffusion coefficient in the modified sample of LCO-Ti/P.

Moreover, the above experimental results indicate the presence of an amorphous Li_3PO_4 coating on the modified sample LCO-Ti/P. Herein, the potential location sites of PO_4^{3-} on the major crystal plane (104) of $LiCoO_2$ were studied, considering three typical sites: (1) the adsorption site by the Li atom, (2) the adsorption site by the Co atom, and (3) the adsorption site midway between Li and Co atoms (Fig. 11a). The calculated adsorption energies are shown in Fig. 11b. The negative adsorption energies suggest that PO_4^{3-} can be easily adsorbed on the (104) plane of $LiCoO_2$.

The oxygen release phenomenon is one of the main problems of the capacity fading of $LiCoO_2$ at high voltage. The effects of PO_4^{3-}adsorption on the formation of an oxygen vacancy were studied, considering four positions of potential oxygen vacancies (O1–O4 in Fig. 11c). In the absence of PO_4^{3-} adsorption, the formation energy for an oxygen vacancy is calculated as − 2.23 eV. The negative formation energy suggests that active oxygen atoms can easily escape from the lattice framework of $LiCoO_2$(104) under a deep delithiation state, which would further lead to structural collapse and more interfacial side reactions. In contrast, in the presence of PO_4^{3-} adsorption, as shown in Fig. 11d, the formation energies of the four types of oxygen vacancies in $LiCoO_2$(104) are positive, indicating that PO_4^{3-}adsorption can inhibit oxygen release from the deep delithiation state of $LiCoO_2$, resulting in superior cycling stability for LCO-Ti/P.

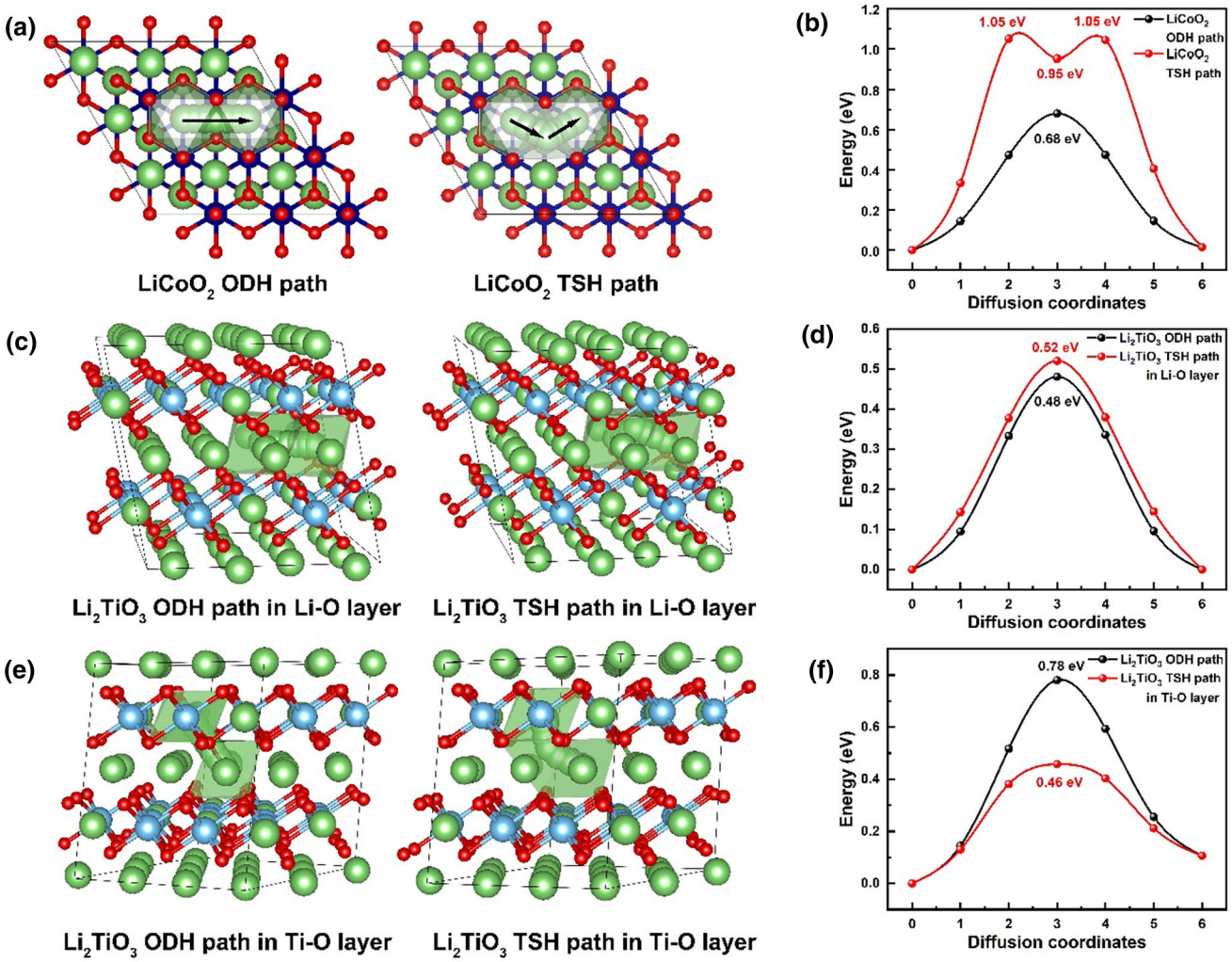

Fig. 10 **a** Schematic diagram of Li-ion diffusion paths in $LiCoO_2$ and **b** the corresponding Li-ion diffusion energy. Li-ion diffusion paths in **c** the Li–O layer and **e** the Ti–O layer of Li_2TiO_3, as well as **d**, **f** the corresponding Li-ion diffusion energies in Li_2TiO_3

Conclusion

A dual-element Ti and P modification method involving a sol–gel treatment and a solid-phase reaction with the precursors of $Ti(OC_4H_9)_4$ and NaH_2PO_2 was developed to improve the electrochemical performance of $LiCoO_2$ at high voltage. The dual-element modified sample LCO-Ti/P shows an initial discharge capacity of 211.6 mAh/g (0.1 C) and excellent capacity retention of 85.7% after 100 cycles at 1 C and RT (3.0–4.6 V). The morphology, phase compositions, and surface microstructure of modified samples were analyzed using SEM, XRD, HRTEM, and XPS to disclose the mechanism for improving the performance at high voltage. It is illustrated that LCO-Ti/P

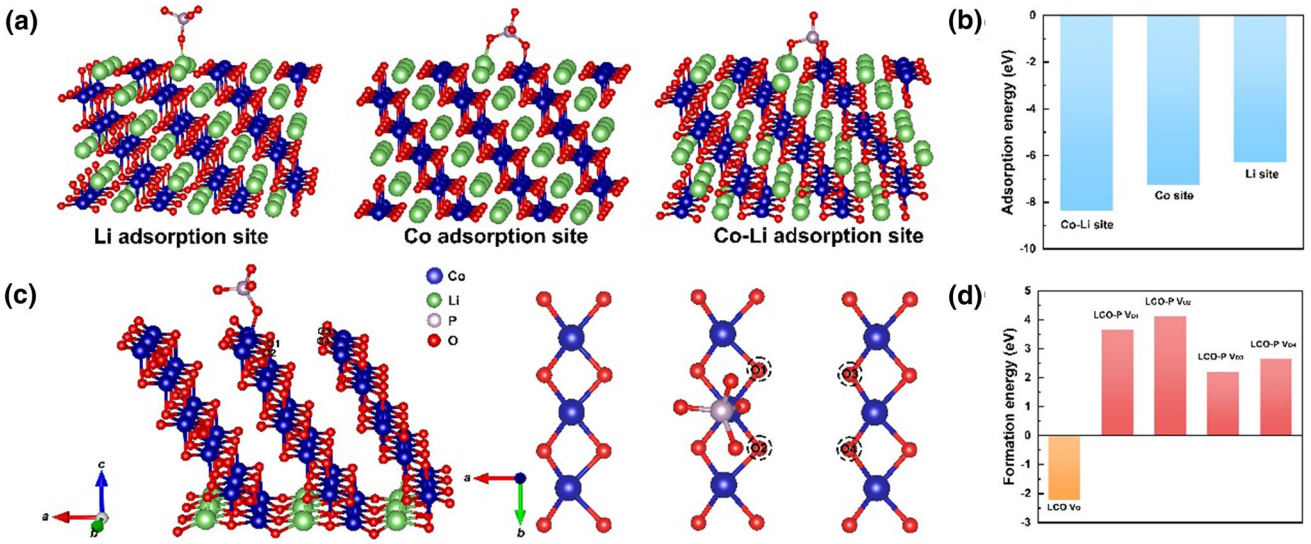

Fig. 11 **a** Initial structure of PO_4^{3-} at three sites on the (104) plane of $LiCoO_2$ and **b** corresponding adsorption energies after optimization. **c** Schematic diagram of the oxygen vacancy position on the (104) plane of $LiCoO_2$ in the presence of one PO_4^{3-} adsorbed at the Co site (denoted as LCO-P). **d** Formation energy for an individual oxygen vacancy located at the position marked by O1, O2, O3, and O4, respectively

has the monoclinic Li_2TiO_3 and the amorphous Li_3PO_4 coating layers. Analyses of in situ XRD, CV, EIS, and GITT tests show that LCO-Ti/P undergoes a mitigated structural change and phase transition. The alleviated growth of charge transfer resistance and an elevated Li-ion diffusion coefficient for LCO-Ti/P stem from the reconstructed interfacial structure. Furthermore, DFT calculations disclose the superior lattice-matching property of the major crystal planes of Li_2TiO_3 and $LiCoO_2$, the lower energy barriers for Li-ion diffusion in Li_2TiO_3, and the suppressed oxygen release performance resulting from the phosphate coating.

Supplementary Information The online version contains supplementary material available at https://doi.org/10.1007/s12209-022-00339-6.

Acknowledgements This work was partially supported by the Major Program of the National Natural Science Foundation of China (No. 22090034). We thank the Haihe Laboratory of Sustainable Chemical Transformations for financial support (CYZC202108).

Declarations

Conflict of interests The authors declare that there is no conflict of interest.

References

1. Wang K, Wan JJ, Xiang YX et al (2020) Recent advances and historical developments of high voltage lithium cobalt oxide materials for rechargeable Li-ion batteries. J Power Sources 460:228062
2. Lyu YC, Wu X, Wang K et al (2021) An overview on the advances of $LiCoO_2$ cathodes for lithium-ion batteries. Adv Energy Mater 11(2):2000982
3. Wang LL, Chen BB, Ma J et al (2018) Reviving lithium cobalt oxide-based lithium secondary batteries-toward a higher energy density. Chem Soc Rev 47(17):6505–6602
4. Zt E, Guo HJ, Yan GC et al (2021) Evolution of the morphology, structural and thermal stability of $LiCoO_2$ during overcharge. J Energy Chem 55:524–532
5. Wan JJ, Zhu JP, Xiang YX et al (2021) Revealing the correlation between structure evolution and electrochemical performance of high-voltage lithium cobalt oxide. J Energy Chem 54:786–794
6. Sharifi-Asl S, Soto FA, Foroozan T et al (2019) Anti-oxygen leaking $LiCoO_2$. Adv Funct Mater 29(23):1901110
7. Fu A, Zhang ZF, Lin JD et al (2022) Highly stable operation of $LiCoO_2$ at cut-off ≥ 4.6 V enabled by synergistic structural and interfacial manipulation. Energy Storage Mater 46:406–416
8. Sun LW, Zhang ZS, Hu XF et al (2019) Realization of Ti doping by electrostatic assembly to improve the stability of $LiCoO_2$ cycled to 4.5 V. J Electrochem Soc 166(10):A1793–A1798

9. Yu JP, Han ZH, Hu XH et al (2014) The investigation of Ti-modified $LiCoO_2$ materials for lithium ion battery. J Power Sources 262:136–139
10. Zou MJ, Yoshio M, Gopukumar S et al (2004) Synthesis and electrochemical performance of high voltage cycling $LiM_{0.05}Co_{0.95}O_2$ as cathode material for lithium rechargeable cells. Electrochem Solid-State Lett 7(7):A176
11. Xu LM, Wang K, Gu F et al (2020) Determining the intrinsic role of Mg doping in $LiCoO_2$. Mater Lett 277:128407
12. Madhavi S, Subba Rao GV, Chowdari BVR et al (2002) Effect of Cr dopant on the cathodic behavior of $LiCoO_2$. Electrochim Acta 48(3):219–226
13. Wang FQ, Jiang Y, Lin SL et al (2019) High-voltage performance of $LiCoO_2$ cathode studied by single particle microelectrodes-influence of surface modification with TiO_2. Electrochim Acta 295:1017–1026
14. Zhou AJ, Lu YT, Wang QJ et al (2017) Sputtering TiO_2 on $LiCoO_2$ composite electrodes as a simple and effective coating to enhance high-voltage cathode performance. J Power Sources 346:24–30
15. Jayasree SS, Nair S, Santhanagopalan D (2018) Ultrathin TiO_2 coating on $LiCoO_2$ for improved electrochemical performance as Li-ion battery cathode. ChemistrySelect 3(10):2763–2766
16. Cho J, Kim YJ, Park B (2000) Novel $LiCoO_2$ cathode material with Al_2O_3 coating for a Li ion Cell. Chem Mater 12(12):3788–3791
17. Scott ID, Jung YS, Cavanagh AS et al (2011) Ultrathin coatings on nano-$LiCoO_2$ for Li-ion vehicular applications. Nano Lett 11(2):414–418
18. Zhou AJ, Liu Q, Wang Y et al (2017) Al_2O_3 surface coating on $LiCoO_2$ through a facile and scalable wet-chemical method towards high-energy cathode materials withstanding high cutoff voltages. J Mater Chem A 5(46):24361–24370
19. Shim JH, Lee SH, Park SS (2014) Effects of MgO coating on the structural and electrochemical characteristics of $LiCoO_2$ as cathode materials for lithium ion battery. Chem Mater 26(8):2537–2543
20. Cho J, Kim YJ, Kim TJ et al (2001) Zero-strain intercalation cathode for rechargeable Li-ion cell. AngewChemInt Ed Engl 40(18):3367–3369
21. Kim YJ, Cho J, Kim TJ et al (2003) Suppression of cobalt dissolution from the $LiCoO_2$ cathodes with various metal-oxide coatings. J Electrochem Soc 150(12):A1723
22. Cho J, Kim TG, Kim C et al (2005) Comparison of Al_2O_3- and $AlPO_4$-coated $LiCoO_2$ cathode materials for a Li-ion cell. J Power Sources 146(1–2):58–64
23. Appapillai AT, Mansour AN, Cho J et al (2007) Microstructure of $LiCoO_2$ with and without "$AlPO_4$" nanoparticle coating: combined STEM and XPS studies. Chem Mater 19(23):5748–5757
24. Zhou AJ, Xu J, Dai XY et al (2016) Improved high-voltage and high-temperature electrochemical performances of $LiCoO_2$ cathode by electrode sputter-coating with Li_3PO_4. J Power Sources 322:10–16
25. Wang CW, Zhou Y, You JH et al (2020) High-voltage $LiCoO_2$material encapsulated in a $Li_4Ti_5O_{12}$ ultrathin layer by high-speed solid-phase coating process. ACS Appl Energy Mater 3(3):2593–2603
26. Lu J, Peng Q, Wang WY et al (2013) Nanoscale coating of $LiMO_2$ (M = Ni Co, Mn) nanobelts with Li^+-conductive Li_2TiO_3: toward better rate capabilities for Li-ion batteries. J Am Chem Soc 135(5):1649–1652
27. Shim JH, Lee J, Han SY et al (2015) Synergistic effects of coating and doping for lithium ion battery cathode materials: synthesis and characterization of lithium titanate-coated $LiCoO_2$ with Mg doping. Electrochim Acta 186:201–208
28. Cui ZZ, Wang ZY, Zhai YW et al (2020) Improving cycling stability and rate capability of high-voltage $LiCoO_2$ through an integration of lattice doping and nanoscale coating. J Nanosci Nanotechnol 20(4):2473–2481
29. Zhu J, Li YJ, Xue LL et al (2019) Enhanced electrochemical performance of Li_3PO_4 modified $Li[Ni_{0.8}Co_{0.1}Mn_{0.1}]O_2$ cathode material via lithium-reactive coating. J Alloys Compd 773:112–120
30. Zhao ZK, Chen S, Mu DB et al (2019) Understanding the surface decoration on primary particles of nickel-rich layered $LiNi_{0.6}Co_{0.2}Mn_{0.2}O_2$ cathode material with lithium phosphate. J Power Sources 431:84–92
31. Wang X, Wu Q, Li SY et al (2021) Lithium-Aluminum-Phosphate coating enables stable 4.6 V cycling performance of $LiCoO_2$ at room temperature and beyond. Energy Storage Mater 37:67–76
32. Gu R, Cheng T, Ma ZT et al (2019) Enhanced cycling stability of high voltage $LiCoO_2$ by surface phosphorylation. J Alloys Compd 803:348–353
33. Kresse G, Furthmüller J (1996) Efficient iterative schemes for ab initio total-energy calculations using a plane-wave basis set. Phys Rev B Condens Matter 54(16):11169–11186
34. Perdew JP, Burke K, Ernzerhof M (1996) Generalized gradient approximation made simple. Phys Rev Lett 77(18):3865–3868
35. Zhang JN, Li QH, Ouyang CY et al (2019) Trace doping of multiple elements enables stable battery cycling of LiCoO2 at 4.6 V. Nat Energy 4(7):594–603
36. Monkhorst HJ, Pack JD (1976) Special points for Brillouin-zone integrations. Phys Rev B 13(12):5188–5192
37. Henkelman G, Uberuaga BP, Jónsson H (2000) A climbing image nudged elastic band method for finding saddle points and minimum energy paths. J Chem Phys 113(22):9901–9904
38. Zhang ZJ, Hu GR, Cao YB et al (2015) Enhanced electrochemical performance of nano $LiMnPO_4$ with multifunctional surface co-coating of Li_2TiO_3 and carbon. Solid State Ion 283:115–122
39. Wang Y, Zhang QH, Xue ZC et al (2020) An in situ formed surface coating layer enabling $LiCoO_2$ with stable 4.6 V high-voltage cycle performances. Adv Energy Mater 10(28):2001413
40. Gu R, Qian RC, Lyu YC et al (2020) One-step integrated comodification to improve the electrochemical performances of high-voltage $LiCoO_2$ for lithium-ion batteries. ACS Sustain Chem Eng 8(25):9346–9355
41. Yang XR, Lin M, Zheng GR et al (2020) Enabling stable high-voltage $LiCoO_2$ operation by using synergetic interfacial modification strategy. Adv Funct Mater 30(43):2004664
42. Nie KH, Sun XR, Wang JY et al (2020) Realizing long-term cycling stability and superior rate performance of 4.5 V-$LiCoO_2$ by aluminum doped zinc oxide coating achieved by a simple wet-mixing method. J Power Sources 470:228423
43. Zhou MJ, Cai LL, Bajdich M et al (2015) Enhancing catalytic CO oxidation over Co_3O_4 nanowires by substituting Co^{2+} with Cu^{2+}. ACS Catal 5(8):4485–4491
44. Sathiyamoorthi R, Chandrasekaran R, Gopalan A et al (2008) Synthesis and electrochemical performance of high voltage cycling $LiCo_{0.8}M_{0.2}O_2$ (M = Mg, Ca, Ba) as cathode material. Mater Res Bull 43(6):1401–1411
45. Ahamed P, Yousuf MA (2020) A novel solid state reaction route to the preparation of $LiCoO_2$ using micro porous filter paper as scaffolds. Mater Res Express 7(6):065506
46. Bian XF, Fu Q, Bie XF et al (2015) Improved electrochemical performance and thermal stability of Li-excess $Li_{1.18}Co_{0.15}Ni_{0.15}Mn_{0.52}O_2$ cathode material by Li_3PO_4 surface coating. Electrochim Acta 174:875–884
47. Wang MJ, Yu FD, Sun G et al (2019) Co-regulating the surface and bulk structure of Li-rich layered oxides by a phosphor doping strategy for high-energy Li-ion batteries. J Mater Chem A 7(14):8302–8314

48. Huang YY, Zhu YC, Fu HY et al (2021) Mg-pillared $LiCoO_2$: towards stable cycling at 4.6 V. Angew Chem Int Ed Engl 60(9):4682–4688
49. Wang YT, Cheng T, Yu ZE et al (2020) Study on the effect of Ni and Mn doping on the structural evolution of $LiCoO_2$ under 4.6 V high-voltage cycling. J Alloys Compd 842:155827
50. Wang LL, Ma J, Wang C et al (2019) A novel bifunctional self-stabilized strategy enabling 4.6 V $LiCoO_2$ with excellent long-term cyclability and high-rate capability. Adv Sci (Weinh) 6(12):1900355
51. Zhang W, Wu YL, Xu ZM et al (2022) Rationally designed sodium chromium vanadium phosphate cathodes with multi-electron reaction for fast-charging sodium-ion batteries. Adv Energy Mater 12(25):2201065
52. Li HX, Xu M, Gao CH et al (2020) Highly efficient, fast and reversible multi-electron reaction of $Na_3MnTi(PO_4)_3$ cathode for sodium-ion batteries. Energy Storage Mater 26:325–333
53. Yang W, Bai CJ, Xiang W et al (2021) Dual-modified compact layer and superficial Ti doping for reinforced structural integrity and thermal stability of Ni-rich cathodes. ACS Appl Mater Interfaces 13(46):54997–55006
54. Zhang P, Xie C, Han G et al (2021) Stable cycling of $LiCoO_2$ at 4.55 V enabled by combined Mg doping and surface coating of NASICON-type electrolyte. Mater Today Nano 15:100122
55. Wang M, Zhang R, Gong YQ et al (2017) Improved electrochemical performance of the $LiNi_{0.8}Co_{0.1}Mn_{0.1}O_2$ material with lithium-ion conductor coating for lithium-ion batteries. Solid State Ion 312:53–60
56. Lee SW, Kim MS, Jeong JH et al (2017) Li_3PO_4 surface coating on Ni-rich $LiNi_{0.6}Co_{0.2}Mn_{0.2}O_2$ by a citric acid assisted Sol-gel method: improved thermal stability and high-voltage performance. J Power Sources 360:206–214
57. Yoon M, Dong YH, Yoo Y et al (2020) Unveiling nickel chemistry in stabilizing high-voltage cobalt-rich cathodes for lithium-ion batteries. AdvFunct Mater 30(6):1907903
58. Zhu Z, Wang H, Li Y et al (2020) A surface Se-substituted $LiCo[O_2–\delta Se\delta]$ cathode with ultrastable high-voltage cycling in pouch full-cells. Adv Mater 32(50):2005182
59. van der Ven A (1999) Lithium diffusion in layered Li_xCoO_2. Electrochem Solid-State Lett 3(7):301
60. Wei Y, Zheng JX, Cui SH et al (2015) Kinetics tuning of Li-ion diffusion in layered $Li(Ni_xMn_yCo_z)O_2$. J Am ChemSoc 137(26):8364–8367

Wei Li is a professor of Tianjin University. Her current research interests focus on modulating the crystal structure and performance of functional materials.